Kaitianite, $Ti^{3+}_2Ti^{4+}O_5$, a new titanium oxide mineral from Allende

Chi MA [iD]* and John R. BECKETT

Division of Geological and Planetary Sciences, California Institute of Technology, Pasadena, California 91125, USA
*Corresponding author. E-mail: chima@caltech.edu

Abstract–Kaitianite, $Ti^{3+}_2Ti^{4+}O_5$, is a new titanium oxide mineral discovered in the Allende CV3 carbonaceous chondrite. The type grain coexists with tistarite (Ti_2O_3) and rutile. Corundum, xifengite, mullite, osbornite, and a new Ti,Al,Zr-oxide mineral are also present, although not in contact. The chemical composition of type kaitianite is (wt%) Ti_2O_3 56.55, TiO_2 39.29, Al_2O_3 1.18, MgO 1.39, FeO 0.59, V_2O_3 0.08 (sum 99.07), yielding an empirical formula of $(Ti^{3+}_{1.75}Al_{0.05}Ti^{4+}_{0.10}Mg_{0.08}Fe_{0.02})(Ti^{4+}_{1.00})O_5$, with Ti^{3+} and Ti^{4+} partitioned, assuming a stoichiometry of three cations and five oxygen anions pfu. The end-member formula is $Ti^{3+}_2Ti^{4+}O_5$. Kaitianite is the natural form of γ-Ti_3O_5 with space group $C2/c$ and cell parameters $a = 10.115$ Å, $b = 5.074$ Å, $c = 7.182$ Å, $\beta = 112°$, $V = 341.77$ Å^3, and $Z = 4$. Both the type kaitianite and associated rutile likely formed as oxidation products of tistarite at temperatures below 1200 K, but this oxidation event could have been in a very reducing environment, even more reducing than a gas of solar composition. Based on experimental data on the solubility of Ti^{3+} in equilibrium with corundum from the literature, the absence of tistarite in or on Ti^{3+}-rich corundum (0.27–1.45 mol% Ti_2O_3) suggests that these grains formed at higher temperatures than the kaitianite (>1579–1696 K, depending on the Ti concentration). The absence of rutile or kaitianite in or on corundum suggests that any exposure to the oxidizing environment producing kaitianite in tistarite was too short to cause the precipitation of Ti-oxides in or on associated corundum.

INTRODUCTION

Fifty years after Allende fell, this CV3 chondrite continues to be a source of new discoveries. Allende has, for example, yielded 19 new minerals since 2007 (Table 1), including numerous examples of refractory and ultra-refractory phases and their alteration products. Each of these new minerals adds a piece to the puzzle of understanding nebular and parent body processes in the early solar system. Here, we describe an occurrence of kaitianite, $Ti^{3+}_2Ti^{4+}O_5$, the latest new mineral to be discovered in Allende.

During an ongoing nanomineralogy investigation of the Allende CV3 carbonaceous chondrite, the new mineral kaitianite, $Ti^{3+}_2Ti^{4+}O_5$ with a $C2/c$ V_3O_5-type structure, was identified in section USNM 3510-5 (Fig. 1) and accorded new mineral status in 2017 by the International Mineralogical Association's Commission on New Minerals, Nomenclature, and Classification (IMA 2017-078a; Ma 2018). Synthetic Ti_3O_5 with the $C2/c$ V_3O_5-type structure is referred to as γ-Ti_3O_5 (Hong and Asbrink 1982; Tanaka et al. 2015).

Ma (2019) gave a preliminary description of the first occurrence of kaitianite, which is expanded in this study. In a brief report, Brearley (1993) reported the occurrence of a fine-grained Ti_3O_5 phase within a chondrite matrix clast in the Nilpena polymict ureilite. This phase has a $C2/m$ Ti_3O_5-type structure (i.e., it is not kaitianite). Ma et al. (2012) described panguite in an Allende ultra-refractory inclusion with a formula of $(Ti^{4+},Al,Sc,Mg,Zr,Ca)_{1.8}O_3$. This phase has a $Pbca$ bixbyite Mn_2O_3-related structure that can be derived from $(Ti^{4+},Al,Sc,Mg,Zr,Ca)_3O_5$. Zhang et al. (2015) observed Sc-rich Ti_3O_5 in an ultra-refractory inclusion from the CH3 chondrite SaU 290. This mineral, which remains unnamed, is distinct from kaitianite because it has a $Cmcm$ pseudobrookite-type structure (in the materials science literature, it is sometimes referred to as anosovite).

Table 1. Nineteen new minerals discovered in the Allende CV3 chondrite since 2007.

IMA no.	Mineral name	Formula	Reference
IMA 2007-027	Allendeite	$Sc_4Zr_3O_{12}$	Ma et al. (2014b)
IMA 2007-029	Hexamolybdenum	(Mo,Ru,Fe)	Ma et al. (2014b)
IMA 2007-033	Monipite	MoNiP	Ma et al. (2014a)
IMA 2008-016	Tistarite	Ti_2O_3	Ma and Rossman (2009a)
IMA 2008-030	Davisite	$CaScAlSiO_6$	Ma and Rossman (2009b)
IMA 2008-042	Grossmanite	$CaTi^{3+}AlSiO_6$	Ma and Rossman (2009c)
IMA 2009-027	Hibonite-(Fe)	$(Fe,Mg)Al_{12}O_{19}$	Ma (2010)
IMA 2010-057	Panguite	$(Ti^{4+},Al,Sc,Mg,Zr,Ca)_{1.8}O_3$	Ma et al. (2012)
IMA 2011-092	Kangite	$(Sc,Ti^{4+},Al,Zr,Mg,Ca,\square)_2O_3$	Ma et al. (2013)
IMA 2012-079	Majindeite	$Mg_2Mo_3O_8$	Ma and Beckett (2016b)
IMA 2013-018	Nuwaite	Ni_6GeS_2	Ma and Beckett (2018)
IMA 2013-029	Hutcheonite	$Ca_3Ti^{4+}{}_2(SiAl_2)O_{12}$	Ma and Krot (2014)
IMA 2013-053	Paqueite	$Ca_3TiSi_2(Al_2Ti)O_{14}$	Ma and Beckett (2016a)
IMA 2013-054	Burnettite	$CaVAlSiO_6$	Ma and Beckett (2016a)
IMA 2014-028	Adrianite	$Ca_{12}(Mg_5Si_9)O_{32}Cl_6$	Ma and Krot (2018)
IMA 2015-001	Beckettite	$Ca_2V_6Al_6O_{20}$	Ma et al. (2016)
IMA 2016-028	Butianite	Ni_6SnS_2	Ma and Beckett (2018)
IMA 2016-110	Rubinite	$Ca_3Ti^{3+}{}_2Si_3O_{12}$	Ma et al. (2017b)
IMA 2017-078	Kaitianite	$Ti^{3+}{}_2Ti^{4+}O_5$	Ma (2019); this study

MINERAL NAME AND TYPE MATERIAL

The name kaitianite is derived from the two Chinese words "Kai Tian," meaning creating the heaven/the sky, from the story of "Pan Gu Kai Tian." In ancient Chinese mythology, the giant Pan Gu created the world by separating the heaven and earth from an egg-shaped chaos. The mineral panguite ([Ti^{4+},Sc,Al, Mg,Zr,Ca]$_{1.8}O_3$; IMA 2010-057, Ma et al. 2012) was named after "Pan Gu" in allusion to the mineral with an ultra-refractory origin being among the first solid materials in the solar system. Type kaitianite formed in the generation following formation of ultra-refractory phases like panguite through oxidation of tistarite, Ti_2O_3, and is part of the overarching story of the early solar system.

The Allende meteorite, which fell near Pueblito de Allende, Chihuahua, Mexico, on February 8, 1969, is a CV3 carbonaceous chondrite. The holotype specimen of kaitianite in Allende section UNSM 3510-5 is in the collections of the Smithsonian Institution's National Museum of Natural History, Washington DC, USA. This section also hosts type tistarite (IMA 2008-016).

ANALYTICAL TECHNIQUES

Electron probe microanalysis (EPMA), high-resolution scanning electron microscopy (SEM), energy-dispersive spectrometer (EDS), and electron backscatter diffraction (EBSD) were used to characterize the composition and structure of the new mineral and associated phases. Backscatter electron (BSE) imaging was performed using a ZEISS 1550VP field emission SEM. EDS analyses were carried out with an Oxford X-Max SDD system and the AZtec program on the ZEISS 1550VP SEM. EBSD analyses were performed using an HKL EBSD system on the ZEISS 1550VP SEM, operated at 20 kV and 6 nA in focused beam mode with a 70° tilted stage and variable pressure mode (25 Pa) using procedures described in Ma and Rossman (2008). The EBSD system was calibrated using a single-crystal silicon standard. The structure was determined and cell constants were obtained by matching the experimental EBSD patterns with all known polymorphs of TiO_2, Magnéli phases (Ti_nO_{2n-1}), Ti_2O_3, Ti_3O_5, and panguite.

Quantitative WDS elemental microanalyses of the type kaitianite and associated tistarite and rutile were carried out using a JEOL 8200 electron microprobe (10 kV and 5 nA, focused beam) on each phase, as marked in Fig. 1b (corundum grains from the crack were also analyzed, but locations are not indicated in Fig. 1). The focused electron beam is ~120 nm in diameter. The interaction volume for X-ray generation in kaitianite is ~500 nm in diameter, estimated using a Casino Monte Carlo simulation of electron trajectory (Drouin et al. 2007). Standards for analysis were anorthite (Al$K\alpha$), fayalite (Fe$K\alpha$), forsterite (Mg$K\alpha$), TiO_2 (Ti$K\alpha$), and V_2O_5 (V$K\alpha$). Analyses were processed with the CITZAF correction procedure (Armstrong 1995) and analytical results are given in Table 2.
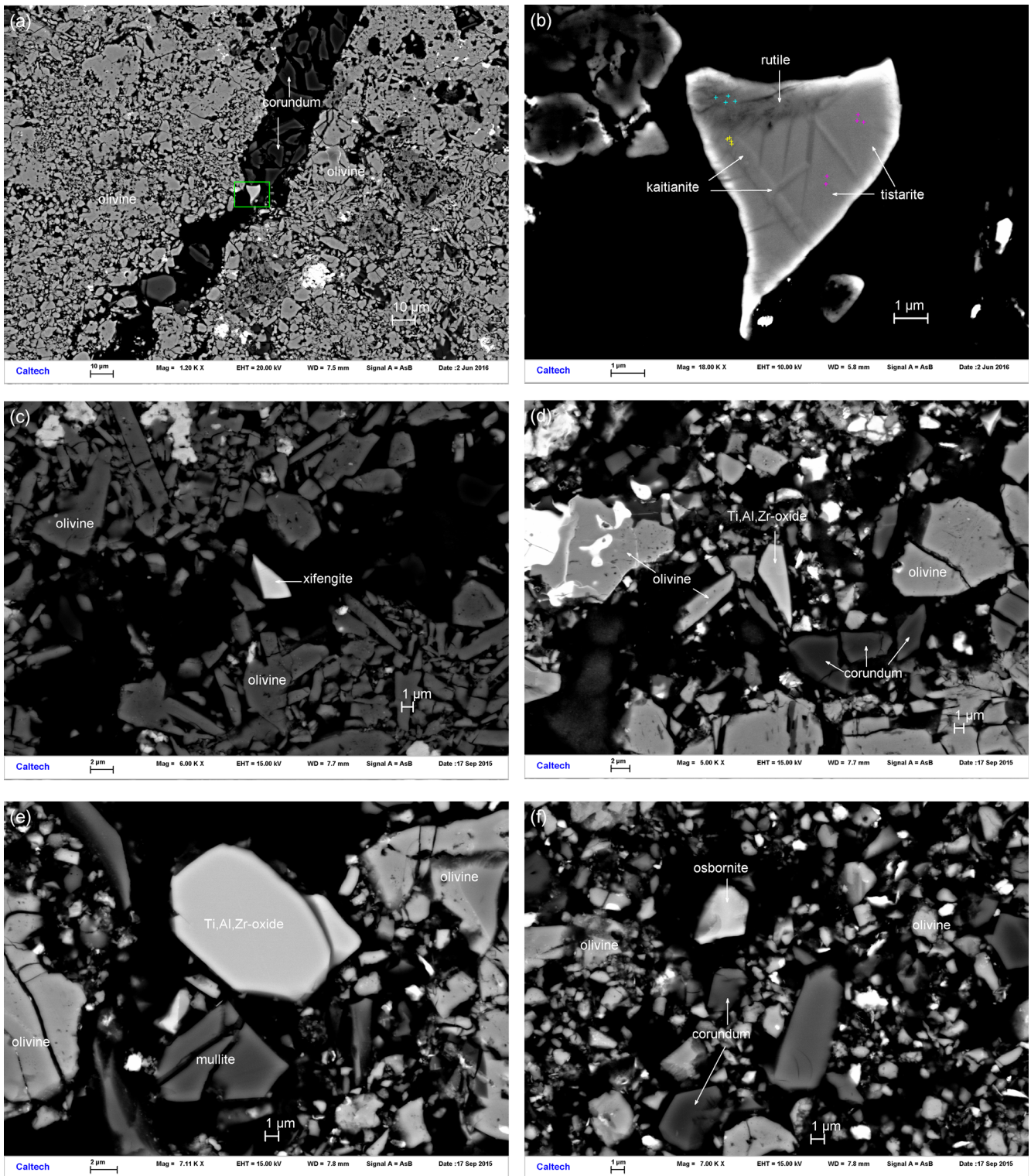
Fig. 1. SEM BSE images showing (a) kaitianite ($Ti^{3+}_2Ti^{4+}O_5$) with tistarite (Ti_2O_3) and rutile (TiO_2) in one grain within the rectangle, along with corundum grains in section USNM 3510-5. b) Close-up of kaitianite. The white boundaries of the grain are an edge effect consequence at the high-current, high-contrast setting. Apparent medium gray needles (in BSE) have no EBSD expression (see Fig. 4). EPMA point analyses (cf. Table 2) are marked with crosses on each phase. c) Close-up of xifengite grain. d) The new Ti,Al,Zr-oxide along with corundum. e) One mullite gain and the new Ti,Al,Zr-oxide. f) One osbornite (TiN) grain with corundum.

Table 2. EPMA results for type kaitianite, associated tistarite (Ti_2O_3) and rutile (TiO_2), and corundum grains in Allende section USNM 3510-5.

Constituent (wt%)	Kaitianite (n = 4)	SD	Tistarite (n = 5)	SD	Rutile (n = 4)	SD	Corundum (n = 20)	SD
Ti_2O_3	56.55*	0.41	95.26	0.52	—		1.28	0.46
TiO_2	39.29*	0.29	—		97.83	0.36	—	
Al_2O_3	1.18	0.11	1.03	0.06	0.3	0.06	98.63	0.87
MgO	1.39	0.1	2.38	0.17	1.35	0.22	0.06	0.03
FeO	0.59	0.04	0.67	0.06	0.59	0.06	0.10	0.08
V_2O_3	0.08	0.11	0.16	0.14	0.38	0.1	na	
Total	99.07		99.5		100.45		100.07	0.61
	Molecular formula							
# Oxygen	5		3		2		3	
Ti^{3+}	1.754		1.903		—		0.018	
Ti^{4+}	1.097		—		0.977		—	
Al	0.052		0.029		0.005		1.980	
Mg	0.077		0.085		0.027		0.001	
Fe	0.018		0.007		0.007		0.001	
V	0.002		0.004		0.004		—	
Sum	3.000		2.033		1.019		2.001	

n = number of analyses; SD = one standard deviation of the mean based on all of the analyses; na = not analyzed.
*Total titanium, which equals 91.91 wt% as Ti_2O_3, has been partitioned between Ti^{3+} and Ti^{4+} in order to make ideal stoichiometry.

RESULTS

Occurrence and Appearance

Kaitianite occurs as two crystals, 0.3 ~ 0.6 μm × 3.6 μm and 0.2 μm × 1.1 μm, in USNM 3510-5 within one irregular grain of tistarite; the kaitianite crystals are in contact with tistarite and rutile (Fig. 1). These Ti-oxides occur together with grains of Ti^{3+}-bearing corundum, xifengite, mullite, osbornite (TiN), and a new Ti,Al,Zr-oxide mineral with composition $(Ti^{3+}_{1.16}Al_{0.57}Zr_{0.11}Si_{0.07}Mg_{0.03})_{\Sigma 1.95}O_3$ (based on three oxygen atoms pfu and assuming all Ti to be trivalent) in several cracks in Allende matrix (Fig. 1), which consists mainly of olivine with minor troilite and pentlandite. The kaitianite composition is nominally consistent with tistarite, but EBSD shows that the crystal structure is distinct (see the Composition and Crystal Structure section). It is related to the structures of panguite and kangite (Ma et al. 2012, 2013) but is, in contrast, highly ordered. We observed no interaction between minerals within the cracks and minerals along the walls of the crack. It seems that the grains were drawn during sample preparation from the same source as a cluster of refractory phases observed in a chondrule in polished thin section USNM 3510-6. In that object, Ti^{3+}-bearing corundum grains occur with mullite, khamrabaevite (TiC), rutile, an Fe-Si alloy, and the type tistarite (Ti_2O_3; IMA 2008-016) (Fig. 2), as described in

Ma and Rossman (2009a) and Ma et al. (2009). We also discovered an example of the new Ti,Al,Zr-oxide mineral in that cluster. USNM 3510-5, which contains the kaitianite, USNM 3510-4, and USNM 3510-6 are adjacent samples from a group of serially sectioned thin sections taken from Allende. The O-isotope analyses of two corundum grains in the cluster in USNM 3510-6 reveal that the grains have compositions well above the terrestrial fractionation line, but they lie on the CCAM line (see fig. 3 of Ma et al. 2009), which is consistent with formation or alteration in an ^{16}O-depleted reservoir within our solar system (i.e., these are probably not presolar grains). Those corundum grains are evidently extraterrestrial materials, not from polishing alumina. Such Ti^{3+}-bearing corundum and associated refractory phases identified in sections USNM 3510-5 and USNM 3510-6 were not found in section USNM 3510-4 under careful examination using the same analytical techniques.

Composition and Crystal Structure

The chemical composition of type kaitianite (Table 2) by low-voltage EPMA (WDS) is (wt%) Ti_2O_3 56.55, TiO_2 39.29, Al_2O_3 1.18, MgO 1.39, FeO 0.59, V_2O_3 0.08, sum 99.07, showing an empirical formula (based on 5 O atoms pfu) of $(Ti^{3+}_{1.75}Al_{0.05}Ti^{4+}_{0.10}Mg_{0.08}Fe_{0.02})(Ti^{4+}_{1.00})O_5$, where Ti^{3+} and Ti^{4+} are partitioned, assuming a stoichiometry with three cations
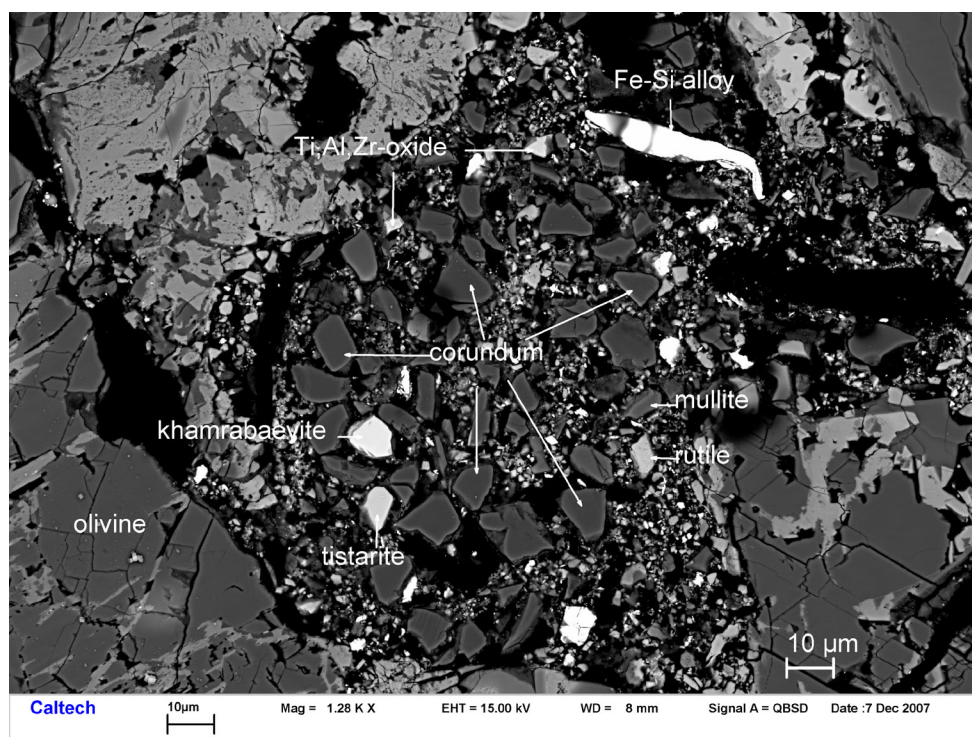
Fig. 2. BSE image showing the cluster of refractory phases corundum, tistarite, rutile, khamrabaevite, mullite, Fe-Si alloy, and the new Ti,Al,Zr-oxide, within a chondrule in USNM 3510-6 (Ma et al. 2009; Ma and Rossman 2009a).

and five oxygen anions pfu. The endmember formula is $Ti^{3+}_2Ti^{4+}O_5$, which requires Ti_2O_3 64.28, TiO_2 35.72, total 100.00 wt%. The empirical formula (based on three oxygen atoms pfu) of associated tistarite is $(Ti^{3+}_{1.90}Mg_{0.08}Al_{0.03}Fe_{0.01})O_3$. The empirical formula (based on two oxygen atoms pfu) of associated rutile is $(Ti^{4+}_{0.98}Mg_{0.03}Fe_{0.01})O_2$.

The EBSD patterns of kaitianite (Fig. 3) could be indexed only by the $C2/c$ V_3O_5-type structure of γ-Ti_3O_5 (Hong and Åsbrink 1982; Tanaka et al. 2015) with a mean angular deviation of 0.33°. For synthetic γ-Ti_3O_5, $a = 10.115$ Å, $b = 5.074$ Å, $c = 7.182$ Å, $β = 112°$, $V = 341.77$ Å^3, and $Z = 4$ (Hong and Åsbrink 1982). X-ray powder diffraction data (Table 3, given in Å for Cu$Kα$1 and Bragg–Brentano geometry) were calculated using Powder Cell version 2.4 (Kraus and Nolze 1996) for the empirical formula from this study and the atomic coordinates of Tanaka et al. (2015), after transforming from $I2/c$ as used by these authors to $C2/c$, the standard setting for Space Group 15. The calculated density is 4.29 g.cm^{-3} using the empirical formula and the above cell parameters.

Kaitianite is isostructural with the minerals oxyvanite (V_3O_5) and berdesinskiite (V_2TiO_5) (Armbruster et al. 2009), as well as synthetic Fe_2TiO_5 and Cr_2TiO_5 with a $C2/c$ V_3O_5-type structure (Drofenik

et al. 1981; Müller-Buschbaum and Bluhm 1988; Pownceby et al. 2001). All of these phases are characterized by two types of octahedral site. One, which contains a 3+ cation, is highly symmetric (Ti-O distances are 2.00–2.04 Å in γ-Ti_3O_5; Hong and Åsbrink 1982). These octahedra share edges and form chains. The second type of cation site forms as pairs of highly distorted face-sharing octahedra (Ti-O distances of 1.88–2.17 Å in γ-Ti_3O_5; Hong and Åsbrink 1982) that are joined to adjacent pairs by shared edges yielding chains that are attached to those of the symmetric octahedra through shared edges.

Associated Minerals

Tistarite and rutile were identified in the grain with kaitianite by EBSD and EPMA (Table 2; Fig. 1b). BSE imaging and EBSD mapping show that kaitianite occurs between rutile and tistarite (Fig. 4) with the rutile forming an ~1 μm layer on one side of the tistarite crystal. Note that there are two- and three-phase contacts, which, as we note below, have important ramifications for origin. There is also nearby corundum (Fig. 1a; Table 2). The corundum grains are not significantly zoned, but there are considerable grain-to-grain variations in Ti (grain averages range from 0.4 to
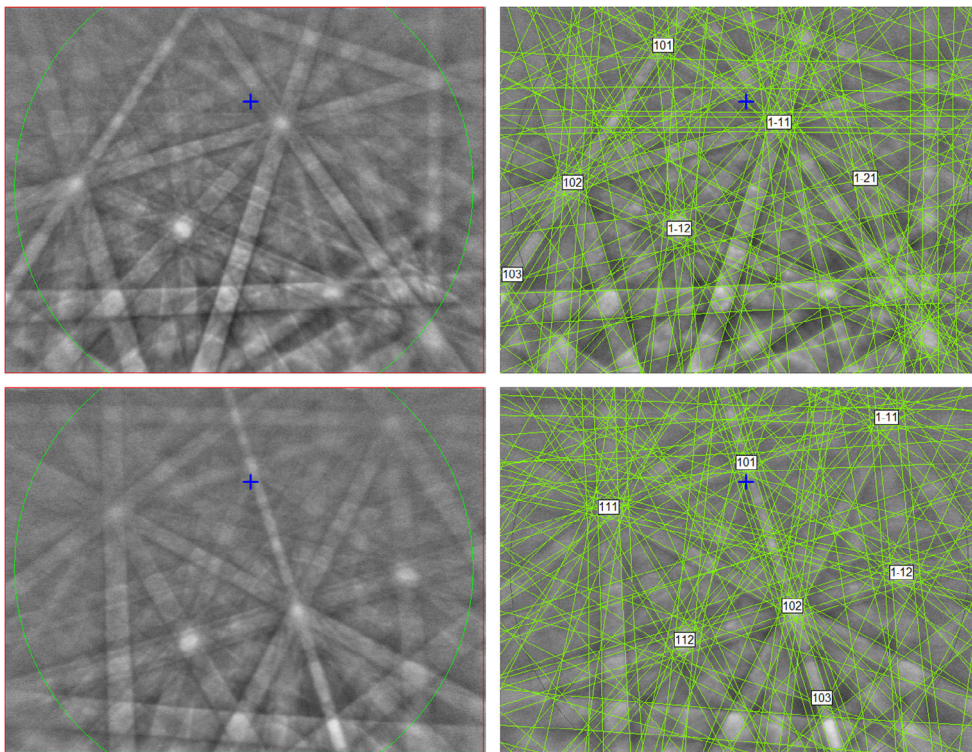
Fig. 3. (Left) EBSD patterns of the larger kaitianite crystal in Fig. 1b, taken at two different orientations, and (right) the patterns indexed with the $C2/c$ γ-Ti_3O_5 structure.

2.0 wt% Ti_2O_3; the composition given in Table 2 is the average of analyses from nine different grains). Ti-bearing xifengite, which was identified by EPMA and EBSD, occurs as one irregular crystal in the crack of the Allende matrix (Fig. 1c) where the kaitianite was found. Its composition by EPMA (wt%) is Fe 69.49, Si 24.83, Ti 3.95, Cr 0.79, V 0.53, total 99.59, showing an empirical formula of $(Fe_{4.45}Ti_{0.30}Cr_{0.05}V_{0.04})Si_{3.16}$. EBSD reveals the phase to have a hexagonal Mn_5Si_3-type xifengite structure. Xifengite has previously been reported in the lunar anorthosite Dho 280 (Nazarov et al. 2015) and in the Khatyrka CV3 meteorite, which contains a variety of iron silicides and Al- and Cu-rich alloys (Lin et al. 2017; Ma et al. 2017a). Ti-bearing mullite, identified by EPMA and EBSD, occurs as one broken euhedral crystal (Fig. 1e), showing an empirical formula of $(Al_{5.61}Ti^{3+}_{0.34}Mg_{0.05})Si_{2.01}O_{13}$. Osbornite (TiN), identified by SEM-EDS and EBSD, occurs as one irregular crystal with corundum grains in a crack of the Allende matrix (Fig. 1f).

We asserted above that the cluster of grains in USNM 3510-6 was likely drawn from the same material as the grains in the crack containing kaitianite shown in Fig. 1. Although this material will be described in a separate publication, we note here that the cluster contains Ti-bearing corundum, mullite, rutile,

khamrabaevite (TiC), and tistarite. If we accept the connection to the occurrence of this study, this phase assemblage places additional constraints on the origin of kaitianite. The cluster in section 3510-6 and the crack in USNM 3510-5 (Figs. 1d, 1e, and 2) also contain a new Ti^{3+}-, Al-, Zr-oxide as irregular-to-euhedral grains with an average empirical formula for the crack occurrence of $(Ti^{3+}_{1.16}Al_{0.57}Zr_{0.11}Si_{0.07}Mg_{0.03})_{\sum 1.95}O_3$ and a general formula of $(Ti^{3+},Al,Zr,Si,Mg)_{1.95}O_3$, assuming all Ti to be Ti^{3+}. Although chemically consistent with tistarite, EBSD (Fig. 5) shows that its crystal structure is distinct. It is related to the structures of panguite and kangite (Ma et al. 2012, 2013) but is, in contrast, highly ordered.

DISCUSSION

Crystal-Chemical Considerations

Kaitianite ($Ti^{3+}_2Ti^{4+}O_5$) is the natural form of γ-Ti_3O_5 and the Ti-analog of oxyvanite (V_3O_5). It is a new member of the berdesinskiite group, which now includes the three minerals berdesinskiite (V_2TiO_5), oxyvanite, and kaitianite. It joins other Ti-rich minerals from carbonaceous chondrites including perovskite, Al.Ti-diopside, tistarite, rutile, grossmanite, davisite,

Table 3. Calculated X-ray powder diffraction data for kaitianite (I_{rel}> 1). The strongest reflections are given in bold.

	k	l	d (Å)	I_{rel}
2	**0**	**0**	**4.6892**	**53**
1	1	0	4.4627	15
−1	1	1	4.0567	1
−2	**0**	**2**	**3.3768**	**75**
0	0	2	3.3295	15
−1	**1**	**2**	**2.9308**	**73**
3	**1**	**0**	**2.6616**	**100**
0	**2**	**0**	**2.5370**	**37**
−3	1	2	2.5048	10
1	**1**	**2**	**2.4662**	**59**
−4	0	2	2.3827	9
0	2	1	2.3708	2
4	0	0	2.3446	6
2	0	2	2.3334	1
−2	2	1	2.2394	28
3	1	1	2.2377	21
2	2	0	2.2314	7
−1	1	3	2.1458	23
−2	2	2	2.0283	29
0	2	2	2.0179	4
−5	1	1	1.8711	1
1	1	3	1.8596	1
−5	1	2	1.8464	1
−2	0	4	1.7951	1
−4	2	1	1.7907	2
5	**1**	**0**	**1.7593**	**49**
−4	**2**	**2**	**1.7368**	**66**
4	2	0	1.7219	6
2	2	2	1.7174	1
−6	0	2	1.6771	1
−3	**1**	**4**	**1.6712**	**67**
0	2	3	1.6705	1
0	0	4	1.6648	13
1	3	0	1.6645	1
−1	1	4	1.6597	5
4	0	2	1.6483	25
6	0	0	1.5631	4
−1	3	2	1.5301	11
−3	3	1	1.5102	1
−5	1	4	1.5008	3
3	3	0	1.4876	25
3	1	3	1.4872	0
1	1	4	1.4760	3
−2	2	4	1.4654	1
−3	3	2	1.4585	2
1	**3**	**2**	**1.4507**	**52**
2	2	3	1.4498	1
−6	0	4	1.4401	7
2	0	4	1.4110	19
0	2	4	1.3919	14
−7	1	2	1.3892	27
4	2	2	1.3822	19

Table 3. *Continued.* Calculated X-ray powder diffraction data for kaitianite (I_{rel}> 1). The strongest reflections are given in bold.

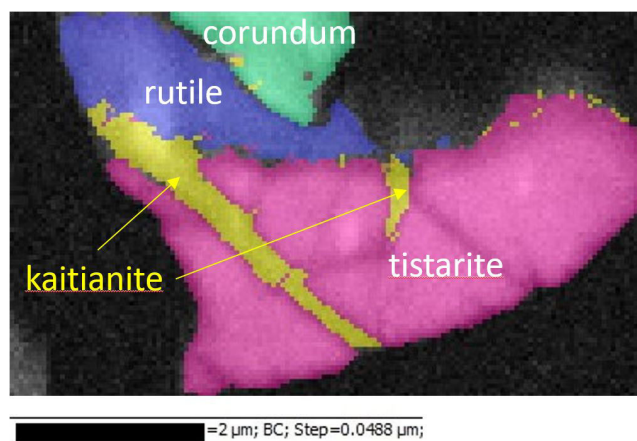|	k	l	d (Å)	I_{rel}
5	1	2	1.3694	1
−7	1	1	1.3678	3
−3	3	3	1.3522	1
−6	2	3	1.3463	2
6	2	0	1.3308	3
−5	1	5	1.3053	3
−5	3	2	1.2867	1
−7	1	4	1.2691	2
0	4	0	1.2685	4
−8	0	2	1.2640	1
5	3	0	1.2561	2
−6	2	4	1.2524	13
0	4	1	1.2461	1
3	1	4	1.2442	2
2	2	4	1.2331	5

Fig. 4. EBSD phase map revealing the occurrence of kaitianite in contact with tistarite and rutile in the Ti-oxide grain. Kaitianite exhibits a lath shape, as shown in the BSE image (Fig. 1b). The EBSD map is apparently deformed due to the highly tilted surface. Corundum near the top of the panel is a different grain.

panguite, kangite, paqueite, zirkelite, tazheranite, rubinite, machiite (Krot et al. 2020), and warkite (Ma et al. 2020). To date, Allende has yielded many Ti^{3+}-rich refractory phases, including grossmanite (Ma and Rossman 2009c), davisite (Ma and Rossman 2009b), rubinite (Ma et al. 2017b), tistarite (Ma and Rossman 2009a), and kaitianite. They formed under extremely
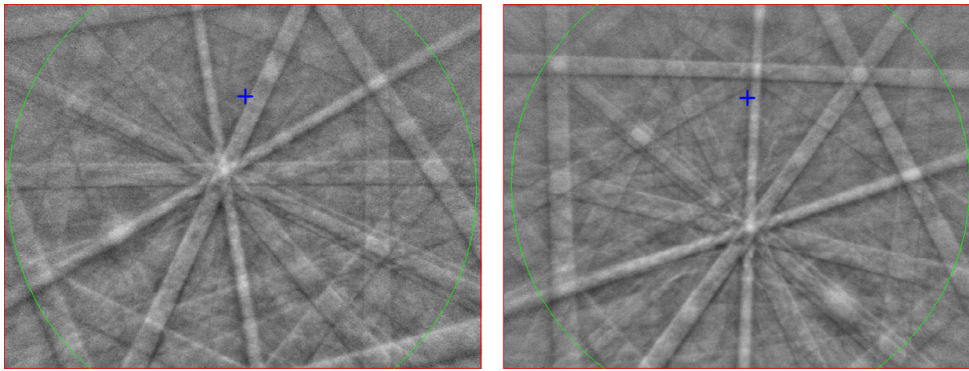
Fig. 5. EBSD patterns of the new Ti,Al,Zr-oxide shown in Figs. 1d and 1e.

reduced environments and survived parent body metamorphism.

Kaitianite is a titanium-oxide, but it contains percent level concentrations of Al_2O_3, MgO, and FeO. An apparent partition coefficient D_i^{j-k}, which refers to the weight ratio of element i between phases j and k, can be constructed from data in Table 2 for elements common to pairs of phases in the kaitianite-bearing grain (i.e., rutile, kaitianite, and tistarite). These show that Al is compatible in kaitianite and tistarite relative to rutile, as might be expected of Ti^{3+}-bearing phases relative to a Ti^{4+}-dominant mineral. All three phases contain significant concentrations of Mg (1.4–2.4 wt% MgO), but tistarite is substantially more magnesian than either kaitianite or rutile, so much so that, if kaitianite and/or rutile formed by the oxidation of tistarite, then Mg was either lost to the oxidizing medium or precipitated in nanocrystals—too small for characterization using the SEM.

Formation Mechanisms and Implications for Nebular Environments

The presence of multiple oxides of Ti and their contacts in the host grain of kaitianite provides some basic constraints on the formation process. Additional phases in the cracks, including the unnamed Ti^{3+}, Al, Zr-oxide, xifengite, mullite, osbornite, and corundum, may also be of help in constraining conditions of formation. We first consider possible constraints on temperature for phases we observed in the crack depicted in Fig. 1a and then focus on redox conditions and process. Rutile, which melts at 2130 K at 1 atm, and tistarite, which melts at 2115 K, are stable over broad ranges in temperature (Chase et al. 1985; Hampl and Schmid-Fetzer 2015). β-Ti_3O_5, the stable high-temperature form of Ti_3O_5, melts incongruently to form Ti_4O_7 at ~1940 K (Hampl and Schmid-Fetzer 2015).

Thus, the mere presence of any of these phases would impose only weak constraints on the temperature of formation. However, the production of kaitianite (γ-Ti_3O_5) likely imposes significant bounds. γ-Ti_3O_5 is generally regarded as a metastable phase (Åsbrink et al. 1971; Hong 1982). During synthesis at high temperatures, above ~1230 K, β-Ti_3O_5 with a pseudobrookite structure is invariably produced. If β-Ti_3O_5, so produced, is then held at progressively lower temperatures, it apparently remains stable until ~450 K, where it undergoes a reversible transition to α-Ti_3O_5. Available thermodynamic data (Chase et al. 1985; Eriksson and Pelton 1993; Waldner and Eriksson 1999; Hampl and Schmid-Fetzer 2015) imply that β-Ti_3O_5 is actually unstable relative to $Ti_2O_3 + Ti_4O_7$ below ~915 K, although this reaction has not, to our knowledge, been observed experimentally. Vapor transport experiments at temperatures in the range of 970–1200 K (e.g., Åsbrink et al. 1971; Hong 1982) often produce γ-Ti_3O_5 (i.e., kaitianite). This phase is thought to be metastable because extended reaction runs sometimes lead to the transformation of γ-Ti_3O_5 to β-Ti_3O_5, but the reverse is not observed. Based on the available synthesis data, it is likely that meteoritic kaitianite formed at temperatures below ~1200 K. If the thermodynamic prediction of $Ti_2O_3 + Ti_4O_7$ stability relative to Ti_3O_5 were to hold in the kinetic environments encountered by kaitianite (i.e., if β-Ti_3O_5 is unstable relative to $Ti_2O_3 + Ti_4O_7$, then γ-Ti_3O_5 is also unstable relative to $Ti_2O_3 + Ti_4O_7$), then the formation of kaitianite would also be restricted to temperatures greater than ~915 K. However, it is possible, even likely, that metastable formation of γ-Ti_3O_5 could be kinetically favored over the stable phase assemblage of $Ti_2O_3 + Ti_4O_7$ to temperatures below 915 K.

The iron silicide xifengite (Fe_5Si_3) has a restricted stability field in the Fe-Si system. According to the

assessment of Cui and Jung (2017), it is only stable between 1090 K, below which it breaks down to the Fe-rich B2 alloy and FeSi, and 1360 K, above which it is unstable relative to Fe_2Si and FeSi. This temperature range (1090–1360 K) overlaps that expected for the production of kaitianite (<~1200 K). If we make the gratuitous assumption that both phases formed under roughly the same conditions, then a formation temperature of 1150 ± ~50 K would account for both phases.

A different type of thermal constraint is implicit in the composition of corundum in USNM 3510-5. Under reducing conditions, up to several mole% Ti is soluble in corundum with a solubility limit, which increases with increasing temperature, dictated by the precipitation of Ti_2O_3 (Fig. 6; Yasuda et al. 1998). Corundum with a particular concentration of Ti_2O_3 can be produced at a temperature higher than this limit (i.e., where the system is undersaturated with respect to tistarite) but not at a lower temperature where tistarite would, at equilibrium, precipitate, thereby lowering the concentration of Ti in the residual corundum to that of the solubility limit. Since we see no evidence for tistarite in or on corundum grains of USNM3510-5, the line in Fig. 6 marks a limiting equilibrium boundary for tistarite-free corundum. Individual grains shown in Fig. 1 contain 0.27–1.45 mol% Ti, a factor of five variation. From Fig. 6, these concentrations translate into minimum temperatures in the range from 1579 (0.27 mol% Ti_2O_3) to 1696 (1.45 mol% Ti_2O_3) K. This result suggests that corundum grains in USNM 3510-5 sampled a variety of environments characterized by significant differences in one or more of temperature, the local activity of Ti, and the oxygen fugacity. They cannot have been produced under nearly identical conditions. The complete absence of tistarite in or on corundum suggests that these grains never equilibrated with tistarite, and in particular, never equilibrated with the tistarite grain shown in Fig. 1. Since the required temperatures for the corundum grains are so much higher than likely formation temperatures for kaitianite (>1579–1696 K versus <1200 K), we can also conclude that the corundum did not equilibrate with kaitianite.

At equilibrium, the Ti-O system contains a wide variety of oxides of varying stoichiometry that are sensitive to redox conditions (e.g., Zador and Alcock 1983; Jacob et al. 2000; Gemelli and Camargo 2007). Rutile, the most oxygen-rich of these, is rare but widely distributed in chondritic meteorites (e.g., Buseck and Keil 1966). Rutile can accommodate a modest concentration of oxygen vacancies charge balancing Ti^{3+} (up to ~0.01 cations pfu) without perturbing the overall crystal structure. However, further loss of oxygen is accomplished through crystallographic shear
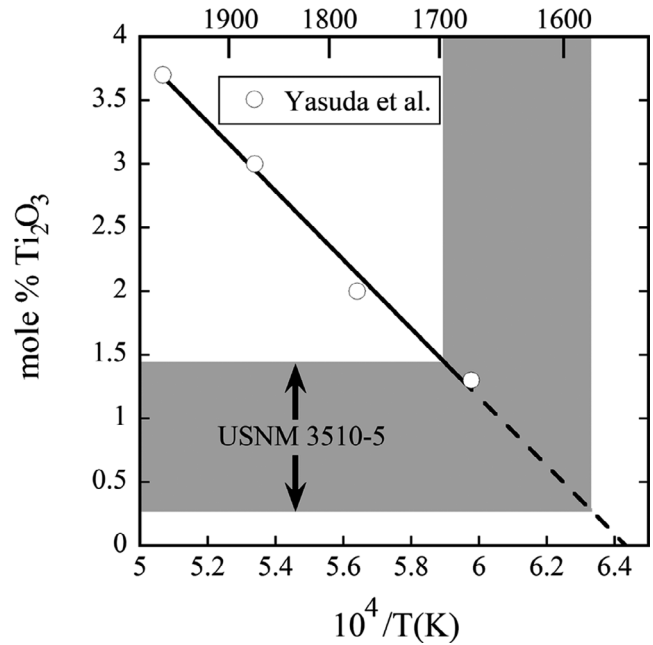

Fig. 6. $10^4/T(K)$ versus mol% Ti_2O_3 in corundum (temperatures in K are indicated on the top axis). Data show temperatures and maximum solubilities according to the data of Yasuda et al. (1998). Gray region indicates minimum temperatures required to account for the observed concentrations of Ti_2O_3 in corundum from USNM 3510-5.

in which a homologous series of "Magnéli phases" with stoichiometry Ti_nO_{2n-1}, where n = 3 to ~28, is produced by the systematic removal of oxygen in planes parallel to the (121) or (132) planes of rutile. This leads to slices n octahedra thick with Ti_2O_3 stoichiometry bounded by rutile-like layers. The oxygen defects are eliminated through this mechanism, but the structure is no longer consistent with that of rutile. Ti_3O_5 is the most reduced of these structures.

We observe rutile–tistarite, rutile–kaitianite, and kaitianite–tistarite contacts in the grain shown in Figs. 1b and 4. No intermediate Magnéli phases are observed. This immediately suggests a nonequilibrium process, as Magnéli phases with n > 3 have stability fields in temperature-oxygen fugacity space that lie between those of TiO_2 and either of Ti_2O_3 or Ti_3O_5 (e.g., Zador and Alcock 1983; Jacob et al. 2000). We would, for equilibrium, not expect direct contacts between kaitianite or tistarite and rutile. We can, nevertheless, compute redox conditions for the stable equilibrium between kaitianite and tistarite via $3Ti_2O_3 + \frac{1}{2}O_2 = 2Ti_3O_5$ and for metastable equilibria involving kaitianite–rutile ($Ti_3O_5 + \frac{1}{2}O_2 = 3TiO_2$) and tistarite–rutile ($Ti_2O_3 + \frac{1}{2}O_2 = 2TiO_2$) using thermodynamic data of Chase et al. (1985). For the first of these three reactions, we have
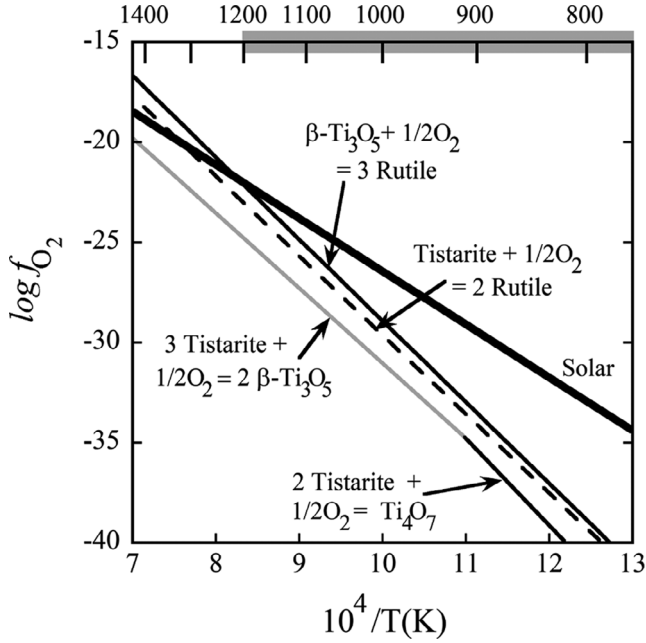
Fig. 7. $10^4/T(K)$ versus $logfO_2$ for selected metastable and stable equilibria of Ti-oxides. Temperatures in K are indicated along the top. Values for equilibrium condensation of a cooling gas of solar composition at a total pressure of 10^{-4} atm (Ebel 2006) are shown for reference. The gray rectangle along the top axis bounds likely temperatures for the formation of γ-Ti$_3$O$_5$ (i.e., $\leq$1200 K).

$$G_\rightarrow = 0 = 2G^\circ_{f,kai} - 3G^\circ_{f,tist} - \frac{1}{2}RT\ln f_{O_2}, \qquad (1)$$

where R is the gas constant, T the temperature, f_{O_2} the oxygen fugacity, $G_\rightarrow$ the free energy of reaction, and $G^\circ_{f,i}$ the free energy of formation of phase i from the constituent elements. Similar expressions can be written for kaitianite–rutile and tistarite–rutile. These equations were solved for $logf_{O_2}$ as a function of inverse temperature and the results are shown in Fig. 7, along with the equilibrium for Ti$_2$O$_3$-Ti$_4$O$_7$ (stable relative to Ti$_3$O$_5$ at temperatures below 915 K, as noted above) and a cooling gas of bulk solar composition at a total pressure of 10^{-4} atm (Ebel 2006). For temperatures below ~1200 K, as expected for the formation of γ-Ti$_3$O$_5$, a grain of tistarite would be susceptible to oxidation, even in a vapor as reducing as gas of solar composition. Of course, more oxidizing redox conditions would also be consistent with oxidation of tistarite. These would include silicate or chondrite dust-enriched nebular systems and planetary environments.

As noted above, Magnéli phases have clear stability fields at Ti/O ratios between those of Ti$_3$O$_5$ and TiO$_2$ (e.g., Zador and Alcock 1983; Jacob et al. 2000). Yet, there are no intermediate Magnéli phases in the kaitianite-bearing grain shown in Fig. 1b and, in particular, there are none between tistarite and rutile. Experimental reduction of rutile (or anatase) consistently produces intermediate Magnéli phases (Lekanova et al. 2003; Chai et al. 2015). Experimental oxidation of Ti metal produces rutile (anatase at low temperatures) with no intermediate Magnéli phases (Gemelli and Camargo 2007). This suggests that the rutile and kaitianite in USNM 3510-5 are much more likely to be oxidation products of tistarite than is tistarite a reduction product of the more oxygen-rich Ti-oxides.

Pravdivtseva et al. (2020) reported the evidence of presolar SiC in an Allende CAI. The presence of TiC in the cluster of grains from USNM 3510-6 described by Ma et al. (2009) makes it tempting to suggest a presolar origin for the grains there and, by extension, the grains observed in USNM 3510-6. TiC is often observed in presolar graphite and calculated to be present in supernova ejecta and in the stellar winds from AGB stars (e.g., Lattimer et al. 1978; Sharp and Wasserburg 1995; Lodders 2006). However, Ma et al. (2009) showed that oxygen isotopic compositions of corundum grains in USNM 3510-6 were consistent with formation in an ^{16}O-depleted reservoir within the solar system and, assuming that the grains USNM 3510-5 and 3510-6 share the same sourcing, this also suggests a solar system origin for grains in USNM 3510-5. Tistarite and Ti-bearing corundum in USNM 3510-5 are nevertheless consistent with formation in an unusually reduced environment. Once formed, these grains were transported to an oxidizing regime where time at temperature was sufficient to partially oxidize tistarite to kaitianite and rutile but insufficient to significantly modify the corundum, which has, thereby, preserved a wide variety of compositions.

CONCLUDING REMARKS

Allende is a key resource for the exploration of processes and environments in the early solar system and it continues to catalyze new insights through measurement and experiment. New Allende phases can be often used as formational probes to add new voices to the chorus raised by previously studied minerals. For example, kaitianite speaks to an oxidation event promulgated on a tistarite grain that formed under extremely reducing conditions. Coexisting rutile also suggests an oxidation event, but the conditions under which kaitianite can form are substantially more restrictive.

REFERENCES

Armbruster T., Galuskin E. V., Reznitsky L. Z., and Sklyarov E. V. 2009. X-ray structural investigation of the oxyvanite (V_3O_5)—berdesinskiite (V_2TiO_5) series: V^{4+} substituting for octahedrally coordinated Ti^{4+}. *European Journal of Mineralogy* 21:885–891.

Armstrong J. T. 1995. CITZAF: A package of correction programs for the quantitative electron microbeam X-ray analysis of thick polished materials, thin films, and particles. *Microbeam Analysis* 4:177–200.

Åsbrink G., Åsbrink S., Magnéli A., Okinaka H., Kosuge K., and Kachi S. 1971. A Ti_3O_5 modification of V_3O_5-type structure. *Acta Chemica Scandinavica* 25:3889–3890.

Brearley A. J. 1993. Occurrence and possible significance of rare Ti oxides (Magnéli phases) in carbonaceous chondrite matrices. *Meteoritics* 28:590–595.

Buseck P. R. and Keil K. 1966. Meteoritic rutile. *American Mineralogist* 51:1506–1515.

Chai G., Huang W., Shi Q., Zheng S., and Wei D. 2015. Preparation and characterization of λ-Ti_3O_5 by carbothermal reduction. *Journal of Alloys and Compounds* 621:404–410.

Chase M. W., Davies C. A., Downey J. R., Frurip D. J., McDonald R. A., and Syverud A. N. 1985. *JANAF thermonuclear tables*, 3rd ed. Washington, D.C.: American Chemical Society.

Cui S. and Jung I.-H. 2017. Critical reassessment of the Fe-Si system. *Calphad* 56:108–125.

Drofenik M., Golič L., Hanžel D., Kraševec V., Prodan A., Bakker M., and Kolar D. 1981. A new monoclinic phase in the Fe_2O_3-TiO_2 system. I. Structure determination and Mössbauer spectroscopy. *Journal of Solid State Chemistry* 40:47–51.

Drouin D., Couture A. R., Joly D., Tastet X., Aimez V., and Gauvin R. 2007. CASINO V2.42—A fast and easy-to-use modeling tool for scanning electron microscopy and microanalysis users. *Scanning* 29:92–101.

Ebel D. S. 2006. Condensation of rocky material in astrophysical environments. In *Meteorites and the early solar system II*, edited by Lauretta D. S. and McSween H. Y. Jr. Tucson, Arizona: University of Arizona Press. pp. 253–277.

Eriksson G. and Pelton A. D. 1993. Critical evaluation and optimization of the thermodynamic properties and phase diagrams of the MnO-TiO_2, MgO-TiO_2, FeO-TiO_2, Ti_2O_3-TiO_2, Na_2O-TiO_2, and K_2O-TiO_2 systems. *Metallurgical Transactions B* 24:795–805.

Gemelli E. and Camargo N. H. A. 2007. Oxidation kinetics of commercially pure titanium. *Revista Matéria* 12:525–531.

Hampl M. and Schmid-Fetzer R. 2015. Thermodynamic description of the Ti-O system. *International Journal of Materials Research* 106:439–453.

Hong S.-H. 1982. Crystal growth of some intermediate titanium oxide phases γ-Ti_3O_5, β-Ti_3O_5, Ti_4O_7 and Ti_2O_3 by chemical transport reactions. *Acta Chemica Scandinavica A* 36:207–217.

Hong S.-H. and Åsbrink S. 1982. The structure of γ-Ti_3O_5 at 297 K. *Acta Crystallographica B* 38:2570–2576.

Jacob K. T., Hoque S. M., and Waseda Y. 2000. Synergistic use of thermogravimetric and electrochemical techniques for thermodynamic study of TiO_x ($1.67 \leq x \leq 2.0$) at 1573 K. *Materials Transactions, JIM* 41:681–689.

Kraus W. and Nolze G. 1996. POWDER CELL—A program for the representation and manipulation of crystal structures and calculation of the resulting X-ray powder patterns. *Journal of Applied Crystallography* 29:301–303.

Krot A. N., Nagashima K., and Rossman G. R. 2020. Machiite, $Al_2Ti_3O_9$, a new oxide mineral from the Murchison carbonaceous chondrite: A new ultra-refractory phase from the solar nebula. *American Mineralogist* 105:239–243.

Lattimer J. M., Schramm D. N., and Grossman L. 1978. Condensation in supernova ejecta and isotopic anomalies in meteorites. *Astrophysical Journal* 219:230–249.

Lekanova T. L., Ryabkov Yu I, and Sevbo O. A. 2003. Particle-size effect on the rate of carbon reduction of TiO_2. *Inorganic Materials* 39:715–719.

Lin C., Hollister L. S., MacPherson G. J., Bindi L., Ma C., Andronicos C. L., and Steinhardt P. J. 2017. Evidence of cross-cutting and redox reaction in Khatyrka meteorite reveals metallic-Al minerals formed in outer space. *Nature Scientific Reports* 7:1637.

Lodders K. 2006. They came from the deep in the supernova: the origin of TiC and metal subgrains in presolar graphite grains. *Astrophysical Journal* 647:L37–L40.

Ma C. 2010. Hibonite-(Fe), $(Fe,Mg)Al_{12}O_{19}$, a new alteration mineral from the Allende meteorite. *American Mineralogist* 95:188–191.

Ma C. 2018. Kaitianite. IMA 2017–078. CNMNC Newsletter No. 42. *Mineralogical Magazine*, 82:445–451.

Ma C. 2019. Discovery of kaitianite, $Ti^{3+}_2Ti^{4+}O_5$, in Allende: A new refractory mineral from the solar nebula. 82nd Annual Meeting of the Meteoritical Society. Abstract no. 6098.

Ma C. and Beckett J. R. 2016a. Burnettite, $CaVAlSiO_6$, and paqueite, $Ca_3TiSi_2(Al_2Ti)O_{14}$, two new minerals from Allende: Clues to the evolution of a V-rich Ca-Al-rich inclusion (abstract #1595). 47th Lunar and Planetary Science Conference. CD-ROM.

Ma C. and Beckett J. R. 2016b. Majindeite, $Mg_2Mo_3O_8$, a new mineral from the Allende meteorite and a witness to post-crystallization oxidation of a Ca-Al-rich refractory inclusion. *American Mineralogist* 101:1161–1170.

Ma C. and Beckett J. R. 2018. Nuwaite (Ni_6GeS_2) and butianite (Ni_6SnS_2), two new minerals from the Allende meteorite: Alteration products in the early solar system. *American Mineralogist* 103:1918–1924.

Ma C. and Krot A. N. 2014. Hutcheonite, $Ca_3Ti_2(SiAl_2)O_{12}$, a new garnet mineral from the Allende meteorite: An alteration phase in a Ca-Al-rich inclusion. *American Mineralogist* 99:667–670.

Ma C. and Krot A. N. 2018. Adrianite, $Ca_{12}(Al_4Mg_3Si_7)O_{32}Cl_6$, a new Cl-rich silicate mineral from the Allende meteorite: An alteration phase in a Ca-Al-rich inclusion. *American Mineralogist* 103:1329–1334.

Ma C. and Rossman G. R. 2008. Barioperovskite, $BaTiO_3$, a new mineral from the Benitoite Mine, California. *American Mineralogist* 93:154–157.

Ma C. and Rossman G. R. 2009a. Tistarite, Ti_2O_3, a new refractory mineral from the Allende meteorite. *American Mineralogist* 94:841–844.

Ma C. and Rossman G. R. 2009b. Davisite, $CaScAlSiO_6$, a new pyroxene from the Allende meteorite. *American Mineralogist* 94:845–848.

Ma C. and Rossman G. R. 2009c. Grossmanite, $CaTi^{3+}AlSiO_6$, a new pyroxene from the Allende meteorite. *American Mineralogist* 94:1491–1494.

Ma C., Beckett J. R., Rossman G. R., Connolly H. C. Jr., Guan Y., Eiler J. M., and Hofmann A. E. 2009. In-situ discovery of a cluster of refractory grains in an Allende ferromagnesian chondrule (abstract# 2138). 40th Lunar and Planetary Science Conference. CD-ROM.

Ma C., Tschauner O., Beckett J. R., Rossman G. R., and Liu W. 2012. Panguite, $(Ti^{4+},Sc,Al,Mg,Zr,Ca)_{1.8}O_3$, a new ultra-refractory titania mineral from the Allende meteorite: Synchrotron micro-diffraction and EBSD. *American Mineralogist* 97:1219–1225.

Ma C., Tschauner O., Beckett J. R., Rossman G. R., and Liu W. 2013. Kangite, $(Sc,Ti,Al,Zr,Mg,Ca,\square)_2O_3$, a new ultrarefractory scandia mineral from the Allende meteorite: Synchrotron micro-Laue diffraction and electron backscatter diffraction. *American Mineralogist* 98:870–878.

Ma C., Beckett J. R., and Rossman G. R. 2014a. Monipite, MoNiP, a new phosphide mineral in a Ca-Al-rich inclusion from the Allende meteorite. *American Mineralogist* 99:198–205.

Ma C., Beckett J. R., and Rossman G. R. 2014b. Allendeite $(Sc_4Zr_3O_{12})$ and hexamolybdenum (Mo,Ru,Fe), two new minerals from an ultrarefractory inclusion from the Allende meteorite. *American Mineralogist* 99:654–666.

Ma C., Paque J., and Tschauner O.2016. Discovery of beckettite, $Ca_2V_6A_{16}O_{20}$, a new alteration mineral in a V-rich Ca-Al-rich inclusion from Allende (abstract #1704). 47th Lunar and Planetary Science Conference. CD-ROM.

Ma C., Lin C., Bindi L., and Steinhardt P. J. 2017a. Hollisterite (Al_3Fe), kryachkoite $(Al,Cu)_6(Fe,Cu)$, and stolperite (AlCu): Three new minerals from the Khatyrka CV3 carbonaceous chondrite. *American Mineralogist* 102:690–693.

Ma C., Yoshizaki T., Krot A.N., Beckett J.R., Nakamura T., Nagashima K., Muto J., Ivanova M.A. 2017b. Discovery of rubinite, $Ca_3Ti^{3+}_2Si_3O_{12}$, a new garnet mineral in refractory inclusions from carbonaceous chondrites. 80th Annual Meeting of the Meteoritical Society, Abstract no. 6023.

Ma C., Krot A. N., Beckett J. R., Nagashima K., Tschauner O., Rossman G. R., Simon S. B., and Bischoff A. 2020. Warkite, $Ca_2Sc_6Al_6O_{20}$, a new mineral in carbonaceous chondrites and a key-stone phase in ultrarefractory inclusions from the solar nebula. *Geochimica et Cosmochimica Acta* 277:52–86.

Müller-Buschbaum H. and Bluhm K. 1988. Weitere magnetische Untersuchungen an $Ti_{(3-x)}M_{(x)}O_5$-Phasen (M = Al^{3+}, Fe^{2+}, Mn^{2+}, Mg^{2+}) mit einem Beitrag uber $CrTi_2O_5$. *Zeitschrift für allgemeine und anorganische Chemie* 558:28–34.

Nazarov M. A., Shornikov S. I., and Demidova S. I. 2015. Origin of native silicon and iron silicides in the Dhofar 280 lunar meteorite. *Petrology* 23:186–194.

Pownceby M. I., Fisher-White M. J., and Swamy V. 2001. Phase relations in the system Fe_2O_3-Cr_2O_3-TiO_2 between 1000 and 1300 °C and the stability of $(Cr,Fe)_2Ti_{n-2}O_{2n-1}$ crystallographic shear structure compounds. *Journal of Solid State Chemistry* 161:45–56.

Pravdivtseva O., Tissot F. L. H., Dauphas N., and Amari S. 2020. Evidence of presolar SiC in the Allende Curious Marie calcium–aluminium-rich inclusion. *Nature Astronomy* 4:617–624.

Sharp C. M. and Wasserburg G. J. 1995. Molecular equilibria and condensation temperatures in carbon-rich gases. *Geochimica et Cosmochimica Acta* 59:1633–1652.

Tanaka K., Nasu T., Miyamoto Y., Ozaki N., Tanaka S., Nagata T., Hakoe F., Yoshikiyo M., Nakagawa K., Umeta Y., Imoto K., Tokoro H., Namai A., and Ohkoshi S. 2015. Structural phase transition between γ-Ti_3O_5 and δ-Ti_3O_5 by breaking of a one-dimensionally conducting pathway. *Crystal Growth & Design* 15:653–657.

Waldner P. and Eriksson G. 1999. Thermodynamic modelling of the system titanium-oxygen. *Calphad* 23:189–218.

Yasuda A., Aoki J., and Sakuma T. 1998. Nanoprecipitation in Al_2O_3-3 mol% Ti_2O_3 due to oxidation. *Ceramics International* 24:483–487.

Zador S. and Alcock C. B. 1983. A thermodynamic study of Magneli and point defect phases in the Ti-O system. *High Temperature Science* 16:187–207.

Zhang A.-C., Ma C., Sakamoto N., Wang R.-C., Hsu W.-B., and Yurimoto H. 2015. Mineralogical anatomy and implications of a Ti-Sc-rich ultrarefractory inclusion from Sayh al Uhaymir 290 CH3 chondrite. *Geochimica et Cosmochimica Acta* 163:27–39.